Jordanian Journal of Computers and Information Technology (JJCIT), Vol. 12, No. 02, June 2026.

ON THE RELIABILITY AND SPECTRAL EFFICIENCY OF MULTI-ANTENNA AF RELAY-AIDED NOMA NETWORKS

Hong-Nhu Nguyen[1], Mui Van Nguyen[2], Minh Xuan Pham[3] and Sang-Quang Nguyen[3]

(Received: 27-Feb.-2026, Revised: 30-Apr.-2026, Accepted: 4-May-2026)

ABSTRACT

This paper investigates a downlink cooperative non-orthogonal multiple access (NOMA) system assisted by a multi-antenna amplify-and-forward (AF) relay. Unlike conventional single-antenna relay configurations, the considered framework jointly exploits relay diversity and direct transmission links between the base station (BS) and users. Under independent Nakagami-k fading channels, closed-form expressions for the outage probability (OP) and ergodic capacity (EC) of both users are derived for scenarios with and without direct BS-user links. The analytical formulation explicitly captures the effects of the number of relay antennas, fading severity and power allocation coefficients on system performance. For the ergodic capacity analysis, an exact integral representation combined with a Gaussian-Chebyshev quadrature approach is developed to efficiently evaluate the performance under the max-SINR selection criterion. The analytical results are verified through Monte-Carlo simulations and compared with orthogonal multiple access (OMA) benchmarks. Numerical results demonstrate that increasing the number of relay antennas significantly improves reliability due to enhanced spatial diversity. Moreover, the NOMA scheme achieves superior outage performance for the far user compared with OMA, while the ergodic capacity of the near user exhibits a pronounced gain in the moderate-to-high SNR regime. These findings confirm the effectiveness of multi-antenna cooperative relaying in improving both reliability and spectral efficiency.

KEYWORDS

Cooperative non-orthogonal multiple access (NOMA), Multi-antenna AF relaying, Spatial diversity, Nakagami-k fading, Outage probability, Ergodic capacity.

1. INTRODUCTION

Driven by the stringent requirements of next-generation wireless networks, non-orthogonal multiple access (NOMA) has emerged as a promising multiple access technique for fifth-generation (5G) and beyond systems [1]-[2]. In NOMA, multiple users are multiplexed in the power domain, where users experiencing poor channel conditions are allocated higher transmit power to guarantee fairness [3]. At the transmitter, superposition coding is employed to combine users' signals, while successive interference cancellation (SIC) is performed at the receivers to extract the desired information [4]. Owing to its flexible architecture, NOMA has also been extended to various emerging communication paradigms, including wireless-powered relaying and secure transmission frameworks [5].

To further enhance coverage and transmission reliability, cooperative NOMA (CNOMA) has been proposed, where relay nodes assist users with unfavorable channel conditions by forwarding the superimposed signals from the base station (BS) [6]-[7]. Relay-assisted transmission is particularly beneficial when the direct link between the BS and the far user suffers from severe path loss or shadowing effects. By introducing cooperative diversity, CNOMA systems can significantly improve reliability compared with non-cooperative NOMA architectures.

In recent years, the integration of NOMA with advanced enabling technologies has attracted increasing attention. For instance, the combination of NOMA and reconfigurable intelligent surfaces (RISs) has been investigated to improve physical layer security and reliability [8]. Active RIS-assisted dual-hop NOMA systems over Nakagami-κ fading channels were analyzed in [9], where closed-form outage and intercept probability expressions were derived to characterize both reliability and secrecy performance. Furthermore, RIS-assisted short-packet NOMA systems were studied in [10], highlighting

1. H.-N. Nguyen is with Faculty of Technology and Eng., Saigon Uni. (SGU), Ho Chi Minh City, Vietnam. Email: nhu.nh@sgu.edu.vn
2. M. V. Nguyen is with Gia Dinh Uni., Ho Chi Minh City, Vietnam. Email: muinv@giadinh.edu.vn
3. M. X. Pham and S.-Q. Nguyen (Corresponding Author) are with Posts and Telecommunications Institute of Technology (PTIT), Ho Chi Minh City, Vietnam. Emails: minhpx@ptit.edu.vn and sangnq@ptit.edu.vn

the impact of finite block-length transmission on secure communication. Beyond infrastructure-based scenarios, RIS-enabled device-to-device (D2D) NOMA frameworks with imperfect SIC were examined in [11], while partial NOMA-assisted backscatter communication systems were investigated in [12] to improve energy efficiency and spectrum utilization. These studies demonstrate the versatility of NOMA when combined with relay technologies, RIS, D2D communication and energy-efficient transmission mechanisms. More recently, several studies have further extended NOMA frameworks toward more practical and performance-oriented communication scenarios. For instance, short-packet NOMA systems have been investigated to support ultra-reliable low-latency communication (URLLC), where the interplay among latency, reliability and secrecy becomes critical under finite blocklength regimes [13]. In parallel, the integration of UAV-assisted communications with SWIPT has been explored to enhance system flexibility and energy efficiency, where joint optimization of power allocation, energy harvesting and UAV deployment plays a key role in improving overall network performance [14]. Moreover, active RIS-enhanced NOMA architectures have been proposed to dynamically reconfigure the wireless propagation environment, enabling both signal amplification and phase adaptation, thereby significantly improving outage performance, throughput and energy efficiency compared with conventional passive designs [15]. In addition, the incorporation of physical layer security and multi-antenna diversity techniques has been shown to effectively enhance robustness against fading and eavesdropping, providing improved secrecy performance in wireless communication systems [16].

These recent developments highlight a clear trend toward more realistic and performance-driven NOMA system designs. However, despite these advances, many existing works focus on integrating specific technologies rather than providing a unified analytical characterization that jointly captures multiple system components.

Despite these advancements, relay-assisted CNOMA systems remain a fundamental and practically relevant architecture due to their deployment simplicity and compatibility with existing networks. Early investigations primarily focused on single-antenna relay configurations [17]-[20], which are attractive for their low hardware complexity. However, single-antenna relays offer limited spatial diversity and interference-suppression capability, leading to performance degradation compared with multi-antenna counterparts [21]-[22]. By contrast, multi-antenna relays can exploit spatial diversity and array gain to significantly enhance transmission reliability and system robustness [23].

In addition to advanced technologies, such as RIS-assisted transmission and DF relaying, amplify-and forward (AF) relay architectures remain highly relevant due to their lower implementation complexity and analytical tractability. In particular, AF relaying avoids signal decoding at the relay, making it suitable for latency-sensitive and resource-constrained systems.

Therefore, the considered multi-antenna AF relay model serves as a canonical and analytically tractable framework for performance evaluation in cooperative NOMA systems. It enables a clear isolation of the gains introduced by cooperative relaying and spatial diversity, thereby providing a meaningful reference for comparison with more advanced, but structurally different, architectures.

Motivated by these benefits, multi-antenna relay-assisted CNOMA systems have been extensively studied under various configurations. A two-user CNOMA system employing a multi-antenna decode-and-forward (DF) relay was analyzed in [24], where outage probability and diversity order were derived in closed form. In [22], a multi-antenna two-way DF relay was considered to improve reliability. The impact of multi-antenna AF/DF relays on secrecy performance was examined in [25], revealing that increasing the number of antennas may introduce complex trade-offs between diversity and information leakage. Multi-antenna downlink NOMA systems were also investigated in [26], where power allocation and feedback overhead were jointly optimized.

Additionally, antenna-and-relay selection strategies were explored in [27]-[28] to reduce implementation complexity while maintaining diversity gains. More recently, full-duplex multi-antenna relaying has been incorporated into CNOMA systems to further enhance spectral efficiency [29]-[30].

Despite the extensive body of work on cooperative and RIS-assisted NOMA systems, existing studies have primarily focused on either decode-and-forward (DF) relaying strategies or RIS-enabled transmission frameworks. Recent works have also considered AF relay-assisted NOMA systems under different design objectives. For instance, the study in [31] investigates an AF relay-aided coordinated direct and relay transmission protocol to enhance energy efficiency and throughput in IoT networks

under imperfect SIC. Meanwhile, the work in [32] focuses on an AF MIMO two-way relay-assisted cognitive radio NOMA system with SWIPT, where secrecy performance is optimized *via* joint beamforming and power allocation.

In particular, multi-antenna DF relay-assisted NOMA works mainly emphasize outage performance, relay/antenna selection and diversity analysis under specific protocol settings [22], [24], while RIS-assisted NOMA approaches typically focus on beamforming design, achievable rate enhancement, SWIPT integration or secure transmission [8][9][10][11][12]. Compared with these studies, existing AF relay-based works are largely oriented toward protocol design or optimization objectives and comprehensive analytical characterizations remain limited.

However, to the best of our knowledge, the joint impact of multi-antenna amplify-and-forward (AF) relaying and direct transmission links on both reliability and spectral efficiency has not been fully characterized in a unified analytical framework. Most existing studies consider either relay-assisted transmission or direct links in isolation, which may not accurately reflect practical deployment scenarios.

To bridge this gap, this paper develops an analytically tractable model for a multi-antenna AF relay assisted NOMA system with MRC/MRT processing, where both direct BS-user links and relay-assisted links are jointly considered. Based on this unified framework, closed-form expressions for outage probability and tractable formulations for ergodic capacity are derived over Nakagami-κ fading channels, enabling a comprehensive characterization of both reliability and spectral efficiency.

The main contributions of this paper are summarized as follows:

- A cooperative NOMA system assisted by a multi-antenna AF relay is formulated, where both direct and relay-assisted transmission links are considered.
- Closed-form analytical expressions for the outage probability and ergodic capacity are derived over Nakagami-κ fading channels and verified *via* Monte-Carlo simulations.
- A comparative analysis is provided by considering OMA and NOMA transmission scenarios with and without direct links and different relay-antenna configurations. These baselines are selected to isolate the performance gains contributed by power-domain multiplexing, relay-assisted transmission and spatial diversity in a unified analytical framework.
- The impacts of transmit signal-to-noise ratio (SNR) and the number of relay antennas on system performance are thoroughly investigated, offering useful insights for practical system design.

Notation: Vectors are denoted by boldface letters, e.g., $\mathbf{x}$. The Frobenius norm is represented by $\|\cdot\|_F$ and $(\cdot)^T$ and $(\cdot)^H$ denote the transpose and Hermitian transpose, respectively.

2. System Architecture and Signal Model

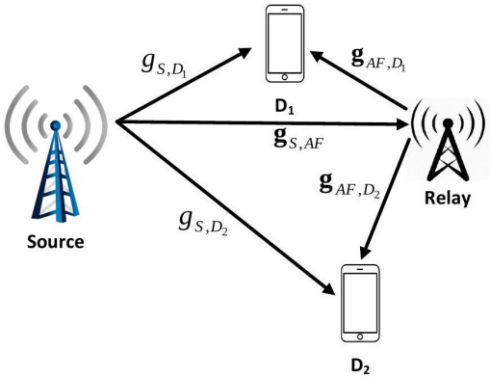

Figure 1. Illustration of the proposed cooperative NOMA architecture.

This section details the system architecture for a downlink cooperative non-orthogonal multiple access (NOMA) network. The layout comprises a single-antenna Source (S) communicating with a pair of single-antenna destinations, labeled as D_1 and D_2. This transmission is facilitated by a half-duplex amplify-and-forward (AF) relay node equipped with an array of K antennas, as depicted in Fig. 1. We assume that all communication links experience mutually independent Nakagami- κ fading. This channel model is adopted due to its flexibility in characterizing a wide range of fading environments,

including the standard Rayleigh fading case as a special scenario. Correspondingly, the channel power gains follow a Gamma distribution, uniquely defined by the severity parameter κ and the average channel gain λ. Additive white Gaussian noise (AWGN) with zero mean and variance σ^2 is assumed to impair all receiving nodes.

Let $\mathbf{g}_{S,AF} \in \mathbb{C}^{K\times 1}$ represent the channel vector spanning from the Source to the K-antenna relay, while $\mathbf{g}_{AF,D_i} \in \mathbb{C}^{K\times 1}$ denotes the link between the relay and destination $D_i (i \in \{1,2\})$. The direct line-of-sight (or non-line-of-sight) channel from the Source to D_i is defined by $g_{S,D_i} \in \mathbb{C}$. Given the Nakagami- κ environment, the respective channel power gains, defined as $|g_{S,D_i}|^2$, $\|\mathbf{g}_{S,AF}\|_F^2$ and $\|\mathbf{g}_{AF,D_i}\|_F^2$, adhere to Gamma distributions. These are parameterized by shape parameters $\kappa_{D_i}, \kappa_{AF}$ and κ_{AF,D_i}, alongside scale parameters (average powers) $\lambda_{D_i}, \lambda_{AF}$ and λ_{AF,D_i}. The noise entities at the relay and users are standard independent complex Gaussian variables, represented by $w_{AF}, w_{D_i} \sim \mathcal{CN}(0, \sigma^2)$.

During the primary transmission stage, the Source broadcasts a combined signal using superposition coding, encompassing two distinct messages s_1 and s_2 associated with the users. Assuming normalized symbol energies $\mathbb{E}[|s_1|^2] = \mathbb{E}[|s_2|^2] = 1$, the broadcast signal is formed as:

$$s_{tx} = \sum_{j=1}^{2} \sqrt{\alpha_j P_S} s_j, \tag{1}$$

where α_1 and α_2 act as the NOMA power allocation factors. To uphold the core NOMA methodology, these coefficients satisfy $\alpha_2 > \alpha_1$ and $\alpha_1 + \alpha_2 = 1$. Consequently, the signal observed at destination D_i is formulated as:

$$r_{D_i} = g_{S,D_i} s_{tx} + w_{D_i}, i \in \{1,2\}. \tag{2}$$

At the AF relay side, a maximum ratio combining (MRC) technique is leveraged. The corresponding receive weight vector is given by:

$$\mathbf{w}_{AF}^H = \frac{\mathbf{g}_{S,AF}^H}{\|\mathbf{g}_{S,AF}\|_F}$$

Therefore, the aggregated baseband signal arriving at the relay takes the form:

$$r_{AF} = \mathbf{w}_{AF}^H \mathbf{g}_{S,AF} s_{tx} + w_{AF}. \tag{3}$$

In the subsequent orthogonal phase, the relay scales and forwards its observed signal as $s_{AF} = \beta r_{AF}$. Here, the variable β denotes the relay amplification factor, strictly chosen to obey the relay's transmit power limit P_{AF}. This factor is computed as:

$$\beta = \sqrt{\frac{P_{AF}}{P_S \|\mathbf{g}_{S,AF}\|_F^2 + \sigma^2}}. \tag{4}$$

It is important to note that the adopted amplification factor corresponds to a variable-gain AF relaying scheme, where the relay gain dynamically adapts to the instantaneous channel state information (CSI) of the source-to-relay link. Compared with fixed-gain AF relaying, this approach effectively mitigates noise amplification and provides better performance in many practical scenarios. Therefore, the adopted model reflects a more realistic relaying operation while preserving the analytical tractability of the derived expressions.

For analytical convenience throughout this work, we presume uniform transmit power across the Source and the relay ($P_{AF} = P_S = P$).

At the relay, maximum ratio combining (MRC) is first applied to the received signal to maximize the received SNR across relay antennas. The combined signal is then amplified and forwarded using maximum ratio transmission (MRT), where the transmit beamforming vector is aligned with the corresponding relay-to-destination channel to enhance the end-to-end link quality.

It is important to note that the relay forwards the amplified version of the superimposed NOMA signal, i.e., the composite signal containing both s_1 and s_2, without performing signal separation or decoding. Therefore, the NOMA superposition structure is preserved across both the direct and relay-assisted links

and the separation of user signals is performed only at the receivers *via* successive interference cancellation (SIC).

For notational convenience, the MRT beamforming vector is expressed with respect to each destination link as $\mathbf{f}_i$, although the relay forwards the same composite signal without performing user-specific precoding.

Accordingly, no explicit multi-user precoding is performed at the relay and MRT is solely used to align the transmitted composite signal with the corresponding relay-to-destination channel, thereby enhancing the effective received SNR.

$$\mathbf{f}_i = \frac{\mathbf{g}_{AF,D_i}}{\left\|\mathbf{g}_{AF,D_i}\right\|_F}, i \in \{1,2\} \tag{5}$$

From a practical implementation perspective, the adopted MRC/MRT processing exploits all available relay antennas to enhance the array and diversity gains. Compared with simpler antenna selection or selection combining (SC) schemes, MRC/MRT requires the channel state information (CSI) of all relay antenna branches and the computation of receive/transmit weighting vectors, resulting in a higher processing burden as the number of relay antennas K increases. However, this complexity remains moderate, since only linear combining and beamforming operations are involved. In contrast, SC provides a lower-complexity alternative by selecting the strongest branch, at the expense of reduced spatial diversity gain. Therefore, MRC/MRT is adopted in this work to fully characterize the reliability and spectral-efficiency benefits of multi-antenna AF relaying.

Consequently, the forwarded signal captured by D_i from the relay node is given by:

$$r_{AF,D_i} = \mathbf{g}_{AF,D_i}^H \mathbf{f}_i s_{AF} + w_{AF,D_i}, i \in \{1,2\}. \tag{6}$$

To streamline the subsequent evaluations, we define the baseline transmit signal-to-noise ratio (SNR) as $\bar{\gamma} = \frac{P}{\sigma^2}$. Let us introduce the random variables $W_i = \left|g_{S,D_i}\right|^2, V = \left\|\mathbf{g}_{S,AF}\right\|_F^2$ and $Q_i = \left\|\mathbf{g}_{AF,D_i}\right\|_F^2$ to capture the channel power gains of the links $S \to D_i, S \to AF$ and $AF \to D_i$. Accordingly, the instantaneous SNRs over these respective paths are $\bar{\gamma}W_i, \bar{\gamma}V$ and $\bar{\gamma}Q_i$.

Due to the NOMA protocol, user D_2 considers the message s_1 as ambient noise. Thus, the instantaneous SINR at D_2 in the first phase is:

$$\Gamma_{D_2} = \frac{\alpha_2 \bar{\gamma} W_2}{\alpha_1 \bar{\gamma} W_2 + 1}. \tag{7}$$

Conversely, user D_1 first detects s_2 to perform successive interference cancellation (SIC). For analytical tractability, ideal SIC is assumed in this work, as commonly adopted in the literature to enable closed-form performance analysis. The SINR at D_1 for extracting s_2 is formulated as:

$$\Gamma_{D_1}^{s_2} = \frac{\alpha_2 \bar{\gamma} W_1}{\alpha_1 \bar{\gamma} W_1 + 1} \tag{8}$$

Accordingly, after successful interference cancellation, the remaining SNR for user D_1 to detect its intended message s_1 simplifies to:

$$\Gamma_{D_1} = \alpha_1 \bar{\gamma} W_1. \tag{9}$$

To account for practical imperfections, in realistic implementations, successive interference cancellation (SIC) may be imperfect due to channel-estimation errors, hardware limitations or residual interference. This effect can be modeled by introducing a residual interference factor $\rho \in [0,1]$, where $\rho = 0$ corresponds to ideal SIC and larger values of ρ indicate more severe residual interference.

In the presence of imperfect SIC, the effective SINR for the near user would be degraded due to the residual interference from the imperfect cancellation of s_2, leading to a higher outage probability and a reduction in ergodic capacity. Nevertheless, the overall performance trends with respect to key system parameters (e.g., the transmit SNR, the number of relay antennas K and the power allocation factors) remain consistent with those observed under the ideal SIC assumption.

Therefore, the ideal SIC assumption adopted in this work provides a useful analytical benchmark, while the above discussion offers practical insights into the impact of SIC imperfections without affecting the generality of the derived results. Regarding CSI, perfect channel knowledge is assumed in the analytical

derivations to maintain closed-form tractability. In practical systems, channel-estimation errors may lead to imperfect CSI and consequently perturb the effective channel gains used in the SINR expressions. Such uncertainty can be incorporated by modeling the estimated channel as the sum of the true channel and an estimation error term, e.g., $\hat{g} = g + e$, where e denotes the estimation error. This extension mainly modifies the effective channel statistics and SINR expressions, while the overall analytical framework remains applicable. A full closed-form treatment under imperfect CSI is left for future work due to the substantially increased analytical complexity. In particular, imperfect CSI typically reduces the effective channel gain and introduces additional uncertainty in the SINR expressions, leading to a performance degradation in both outage probability and ergodic capacity. Moving to the second phase, incorporating the amplification scalar and the MRT scheme, the end-to-end SINR at D_2 to retrieve s_2 *via* the relay path is calculated by:

$$\Gamma_{AF,D_2}^{s_2} = \frac{\alpha_2 \bar{\gamma}^2 V Q_2}{\alpha_1 \bar{\gamma}^2 V Q_2 + \bar{\gamma} V + \bar{\gamma} Q_2 + 1}. \tag{10}$$

Similarly, focusing on the $AF \to D_1$ cascade, the SINR at D_1 for the initial detection of s_2 and the subsequent SNR to decode its own data s_1, are represented, respectively, as:

$$\Gamma_{AF,D_1}^{s_2} = \frac{\alpha_2 \bar{\gamma}^2 V Q_1}{\alpha_1 \bar{\gamma}^2 V Q_1 + \bar{\gamma} V + \bar{\gamma} Q_1 + 1}, \tag{11}$$

$$\Gamma_{AF,D_1}^{s_1} = \frac{\alpha_1 \bar{\gamma}^2 V Q_1}{\bar{\gamma} V + \bar{\gamma} Q_1 + 1}. \tag{12}$$

Operating under a selection combining (SC) strategy, the ultimate effective SINRs available at destinations D_2 and D_1 are written as:

$$\Gamma_{D_2}^{eff} = \max\left(\Gamma_{D_2}, \Gamma_{AF,D_2}^{s_2}\right), \tag{13a}$$

$$\Gamma_{D_1}^{eff} = \max\left(\Gamma_{D_1}, \Gamma_{AF,D_1}^{s_1}\right). \tag{13b}$$

Although identical noise variance and representative large-scale fading parameters are adopted for clarity in the numerical evaluation, the proposed analytical framework remains sufficiently general to accommodate more realistic scenarios. In particular, heterogeneous settings with unequal path-loss and noise power across different links can be readily incorporated by appropriately adjusting the corresponding channel statistics. Therefore, such generalizations do not alter the fundamental structure of the derived expressions or the main performance insights.

3. PERFORMANCE METRICS ANALYSIS

3.1 Outage-probability Analysis

Given the nature of half-duplex relay networks, an entire communication cycle demands two orthogonal time slots. To guarantee specific quality-of-service (QoS) demands, the target SINR bounds for our nodes are mapped as:

$$\tau_{th,i} = 2^{2R_i} - 1, i \in \{1,2\},$$

where R_i indicates the pre-defined spectral efficiency threshold for D_i.

3.1.1 Outage Probability for Node D_2

Drawing upon standard literature [34]-[35], the cumulative distribution functions (CDFs) dictating the behavior of random variables W_i, V and Q_i are documented as:

$$F_{W_i}(x) = 1 - e^{-\eta_{D_i} x} \sum_{u=0}^{\kappa_{D_i}-1} \frac{\eta_{D_i}^u x^u}{u!}, i \in \{1,2\} \tag{14a}$$

$$F_V(x) = 1 - e^{-\eta_{AF} x} \sum_{u=0}^{\kappa_{AF}K-1} \frac{\eta_{AF}^u x^u}{u!} \tag{14b}$$

$$F_{Q_i}(x) = 1 - e^{-\eta_{AF,D_i} x} \sum_{u=0}^{\kappa_{AF,D_i}K-1} \frac{\eta_{AF,D_i}^u x^u}{u!}, i \in \{1,2\} \tag{14c}$$

The related probability density functions (PDFs) follow the shapes below:

$$f_{W_i}(x) = \frac{\eta_{D_i}^{\kappa_{D_i}}}{\Gamma(\kappa_{D_i})} x^{\kappa_{D_i}-1} e^{-\eta_{D_i} x}, i \in \{1,2\} \quad (15a)$$

$$f_V(x) = \frac{\eta_{AF}^{\kappa_{AF}K}}{\Gamma(\kappa_{AF}K)} x^{\kappa_{AF}K-1} e^{-\eta_{AF} x} \quad (15b)$$

$$f_{Q_i}(x) = \frac{\eta_{AF,D_i}^{\kappa_{AF,D_i}K}}{\Gamma(\kappa_{AF,D_i}K)} x^{\kappa_{AF,D_i}K-1} e^{-\eta_{AF,D_i} x}, i \in \{1,2\} \quad (15c)$$

Here, the constants are $\eta_{D_i} = \frac{\kappa_{D_i}}{\lambda_{D_i}}, \eta_{AF} = \frac{\kappa_{AF}}{\lambda_{AF}}$ and $\eta_{AF,D_i} = \frac{\kappa_{AF,D_i}}{\lambda_{AF,D_i}}$.

The outage likelihood for user D_2 evaluates the probability that its effective SINR falls short of the target τ_{th}:

$$O_2 = \Pr\left(\Gamma_{D_2}^{eff} < \tau_{th}\right) = \Pr\left(\max\left(\Gamma_{D_2}, \Gamma_{AF,D_2}^{S_2}\right) < \tau_{th}\right)$$
$$= \underbrace{\Pr\left(\Gamma_{D_2} < \tau_{th}\right)}_{\Psi_1} \underbrace{\Pr\left(\Gamma_{AF,D_2}^{S_2} < \tau_{th}\right)}_{\Psi_2} \quad (16)$$

The exact closed-form metric for D_2 's outage probability is derived as:

$$O_2 = \left(1 - e^{-\eta_{D_2}\vartheta} \sum_{u=0}^{\kappa_{D_2}-1} \frac{\eta_{D_2}^u \vartheta^u}{u!}\right) \times \left\{1 - 2 \sum_{v=0}^{\kappa_{AF}K-1} \sum_{j=0}^{v} \sum_{l=0}^{\kappa_{AF,D_2}K-1} \binom{v}{j} \binom{\kappa_{AF,D_2}K-1}{l} \right.$$
$$\times \frac{\eta_{AF}^v (\vartheta^2 + \vartheta\bar{\gamma}^{-1})^j \vartheta^{-(\kappa_{AF,D_2}K+v-j-l-1)} e^{-\vartheta(\eta_{AF,D_2}+\eta_{AF})}}{v!\,\Gamma(\kappa_{AF,D_2}K)}$$
$$\left. \times \eta_{AF,D_2}^{\kappa_{AF,D_2}K} \left(\frac{\eta_{AF}(\vartheta^2 + \vartheta\bar{\gamma}^{-1})}{\eta_{AF,D_2}}\right)^{\frac{l-j+1}{2}} \times K_{l-j+1}\left(2\sqrt{\eta_{AF}\eta_{AF,D_2}(\vartheta^2 + \vartheta\bar{\gamma}^{-1})}\right)\right\} \quad (17)$$

with the condition threshold defined as:

$$\vartheta = \frac{\tau_{th}}{\bar{\gamma}(\alpha_2 - \alpha_1\tau_{th})}$$

Proof 1. Refer to Appendix A.

3.1.2 Outage Probability for Node D_1

By a similar logic, D_1 's probability of communication failure is deduced as:

$$O_1 = \Pr\left(\Gamma_{D_1}^{eff} < \tau_{th}\right) = \Pr\left(\max\left(\Gamma_{D_1}, \Gamma_{AF,D_1}^{S_1}\right) < \tau_{th}\right) \quad (18)$$

Exploiting the statistical independence between the direct and relayed routes, we decompose the formula into:

$$O_1 = \underbrace{\Pr\left(\Gamma_{D_1} < \tau_{th}\right)}_{\Xi_1} \underbrace{\Pr\left(\Gamma_{AF,D_1}^{S_1} < \tau_{th}\right)}_{\Xi_2} \quad (19)$$

Computation of Ξ_1

Reflecting on $\Gamma_{D_1} = \alpha_1\bar{\gamma}W_1$, the failure state translates to:

$W_1 < \phi$, where we substitute $\phi = \frac{\tau_{th}}{\alpha_1\bar{\gamma}}$

Thus, the first term evaluates to:

$$\Xi_1 = F_{W_1}(\phi) = 1 - e^{-\eta_{D_1}\phi} \sum_{u=0}^{\kappa_{D_1}-1} \frac{\eta_{D_1}^u \phi^u}{u!} \quad (20)$$

Computation of Ξ_2

Referring back to (12), the boundary $\Gamma_{AF,D_1}^{S_1} < \tau_{th}$ algebraically shifts to:

$$VQ_1 < \phi(V + Q_1 + \bar{\gamma}^{-1})$$

A minor rearrangement isolates:

$$V < \frac{\phi(Q_1 + \bar{\gamma}^{-1})}{Q_1 - \phi}, \text{ under the premise } Q_1 > \phi.$$

As such, we formulate the probability integral:

$$\Xi_2 = 1 - \int_{\phi}^{\infty} f_{Q_1}(y)\left[1 - F_V\left(\frac{\phi(y + \bar{\gamma}^{-1})}{y - \phi}\right)\right]dy \tag{21}$$

Inserting the predefined mathematical distributions into (21) results in:

$$\Xi_2 = 1 - \sum_{p=0}^{\kappa_{AF}K-1} \frac{\eta_{AF,D_1}^{\kappa_{AF,D_1}K}\eta_{AF}^{p}}{p!\,\Gamma\left(\kappa_{AF,D_1}K\right)} \times \int_{\phi}^{\infty} y^{\kappa_{AF,D_1}K-1}e^{-\eta_{AF,D_1}y}e^{-\eta_{AF}\frac{\phi(y+\bar{\gamma}^{-1})}{y-\phi}}\left(\frac{\phi(y + \bar{\gamma}^{-1})}{y - \phi}\right)^{p}dy \tag{22}$$

Deploying variable substitution $z = y - \phi$ (thus $= z + \phi$), the equation morphs into:

$$\Xi_2 = 1 - \sum_{p=0}^{\kappa_{AF}K-1} \frac{\eta_{AF,D_1}^{\kappa_{AF,D_1}K}\eta_{AF}^{p}e^{-\phi(\eta_{AF,D_1}+\eta_{AF})}}{p!\,\Gamma\left(\kappa_{AF,D_1}K\right)} \times \int_{0}^{\infty} (z+\phi)^{\kappa_{AF,D_1}K-1}e^{-\eta_{AF,D_1}z}e^{-\frac{\eta_{AF}\phi(\phi+\bar{\gamma}^{-1})}{z}}\left(\phi + \frac{\phi^2 + \phi\bar{\gamma}^{-1}}{z}\right)^{p}dz \tag{23}$$

By utilizing the standard integral tables from ([33], Eq. (1.111), (3.471.9)), the integration can be entirely resolved. Skipping tedious algebra, the explicit closed-form result is:

$$\Xi_2 = 1 - 2\sum_{p=0}^{\kappa_{AF}K-1}\sum_{w=0}^{p}\sum_{l=0}^{\kappa_{AF,D_1}K-1}\binom{p}{w}\binom{\kappa_{AF,D_1}K-1}{l} \times \frac{\eta_{AF}^{p}\eta_{AF,D_1}^{\kappa_{AF,D_1}K}e^{-\phi(\eta_{AF,D_1}+\eta_{AF})}}{p!\,\Gamma\left(\kappa_{AF,D_1}K\right)}(\phi^2 + \phi\bar{\gamma}^{-1})^{w}\phi^{\kappa_{AF,D_1}K+p-w-l-1} \times \left(\frac{\eta_{AF}(\phi^2 + \phi\bar{\gamma}^{-1})}{\eta_{AF,D_1}}\right)^{\frac{l-w+1}{2}} K_{l-w+1}\left(2\sqrt{\eta_{AF}\eta_{AF,D_1}(\phi^2 + \phi\bar{\gamma}^{-1})}\right). \tag{24}$$

Ultimately, aggregating (20) and (24) into (19) yields the final outage equation for D_1.

3.1.3 High-SNR and Feasibility Insights

The derived outage expressions also provide useful insights into the high-SNR behavior and feasibility of the considered NOMA transmission. From the threshold variable $\vartheta = \frac{\tau_{\text{th}}}{\bar{\gamma}(\alpha_2 - \alpha_1\tau_{\text{th}})}$, it is clear that successful decoding of the far-user signal requires the feasibility condition $\alpha_2 > \alpha_1\tau_{th}$.

Equivalently, since $\alpha_1 + \alpha_2 = 1$, this condition can be written as $\alpha_2 > \tau_{\text{th}}/(1 + \tau_{\text{th}})$. If this condition is not satisfied, the required SINR threshold cannot be achieved even when the transmit SNR becomes large, which leads to an unavoidable outage floor for the far-user stream.

For the near user, the decoding of its own signal after successful SIC requires $\alpha_1 > 0$, while the prior decoding of the far-user message at D_1 follows the same feasibility condition $\alpha_2 > \alpha_1\tau_{th}$. Therefore, the power-allocation coefficients and target SINR threshold must be jointly selected to ensure meaningful outage performance for both users.

In the high-SNR regime, the outage probability generally follows the form $O_i \propto \bar{\gamma}^{-d_i}$, where d_i denotes the diversity order. Based on the small-argument behavior of the Gamma-distributed channel gains, the direct link contributes a diversity term governed by κ_{D_i}, whereas the relay-assisted path is mainly governed by the weaker hop between the $S \to AF$ and $AF \to D_i$ links, i.e., approximately $\min\left(\kappa_{AF}K, \kappa_{AF,D_i}K\right)$. Hence, under selection combining with both direct and relay-assisted links, the effective diversity order can be interpreted as:

$$d_i \approx \kappa_{D_i} + \min\left(\kappa_{AF}K, \kappa_{AF,D_i}K\right).$$

This observation explains why increasing the number of relay antennas K steepens the outage curves in the high-SNR region. Under the common fading-severity setting used in the simulations, this diversity gain increases approximately linearly with K, which is consistent with the trends observed in Figs. 2-3.

3.2 Ergodic-capacity Evaluation

We commence by formalizing the ergodic capacity function for the far node (D_2) :

$$C_{D_2} = \mathbb{E}\left\{\frac{1}{2}\log_2\left(1+\Gamma_{D_2}^{eff}\right)\right\} = \mathbb{E}\left\{\frac{1}{2}\log_2\left(1+\max\left(\Gamma_{D_2},\Gamma_{AF,D_2}^{S_2}\right)\right)\right\}. \tag{25}$$

The analytical closed-form representation of D_2 's capacity is resolved as:

$$\begin{aligned} C_{D_2} = \frac{1}{2\ln 2}\Bigg\{ & \sum_{u=0}^{\kappa_{D_2}-1} \frac{\eta_{D_2}^u}{u!\,\bar{\gamma}^u}\left[\frac{1}{(\alpha_2+\alpha_1)^u} G_{1,2}^{2,1}\left(\frac{\eta_{D_2}}{\bar{\gamma}(\alpha_2+\alpha_1)}\middle| \begin{matrix} 1-u-1,- \\ 1-u-1,0 \end{matrix}\right)\right. \\ & \left. - \frac{1}{\alpha_1^u} G_{1,2}^{2,1}\left(\frac{\eta_{D_2}}{\bar{\gamma}\alpha_1^u}\middle| \begin{matrix} 1-u-1,- \\ 1-u-1,0 \end{matrix}\right)\right] + \frac{\pi^2}{2D} \sum_{v=0}^{\kappa_{AF}K-1} \sum_{j_1=0}^{v} \sum_{j_2=0}^{\kappa_{AF,D_2}K-1} \sum_{d=1}^{D} \binom{v}{j_1} \Bigg\} \\ & \times \binom{\kappa_{AF,D_2}K-1}{j_2} \frac{\eta_{AF,D_2}^{\kappa_{AF,D_2}} \eta_{AF}^{v} \sqrt{1-\Omega_d^2}}{v!\,\Gamma\left(\kappa_{AF,D_2}K\right)} \sec^2\left(\frac{\pi}{4}(\Omega_d+1)\right) \\ & \times \left(\frac{1}{\Upsilon(\Omega_d)+(\alpha_2+\alpha_1)^{-1}} - \frac{1}{\Upsilon(\Omega_d)+\alpha_1^{-1}}\right) \Theta(\Omega_d)^{j_1} \\ & \times \left(1 - e^{-\frac{\eta_{D_2}\Upsilon(\Omega_d)}{\bar{\gamma}}} \sum_{u=0}^{\kappa_{D_2}-1} \frac{\eta_{D_2}^u \Upsilon(\Omega_d)^u}{u!\,\bar{\gamma}^u}\right) \left(\frac{\Upsilon(\Omega_d)}{\bar{\gamma}}\right)^{\kappa_{AF,D_2}K+v-j_1-j_2-1} \\ & \times e^{-\frac{\Upsilon(\Omega_d)(\eta_{AF,D_2}+\eta_{AF})}{\bar{\gamma}}} \left(\frac{\eta_{AF}\Theta(\Omega_d)}{\eta_{AF,D_2}}\right)^{\frac{j_2-j_1+1}{2}} K_{j_2-j_1+1}\left(2\sqrt{\eta_{AF}\eta_{AF,D_2}\Theta(\Omega_d)}\right)\Bigg\} \end{aligned} \tag{26}$$

where the roots for the Gaussian-Chebyshev approximation are:

$$\Omega_d = \cos\left(\frac{2d-1}{2D}\pi\right), d = 1, \ldots, D$$

and the auxiliary variables stand for:

$$\Upsilon(\Omega_d) = \tan\left(\frac{\pi(\Omega_d+1)}{4}\right), \Theta(\Omega_d) = \frac{\Upsilon(\Omega_d)}{\bar{\gamma}^2}(\Upsilon(\Omega_d)+1)$$

Proof 3. Refer to Appendix B for full derivations.

Progressing to the near node, the average capacity for D_1 is captured by:

$$\begin{aligned} C_{D_1} &= \mathbb{E}\left\{\frac{1}{2}\log_2\left(1+\Gamma_{D_1}^{eff}\right)\right\} = \mathbb{E}\{\frac{1}{2}\log_2(1+\underbrace{\max\left(\Gamma_{D_1},\Gamma_{AF,D_1}^{S_1}\right)}_{U_{\text{var}}})\} \\ &= \frac{1}{2\ln 2}\int_0^{\infty} \frac{1}{1+y}\left[1-F_{U_{\text{var}}}(y)\right]dy \end{aligned} \tag{27}$$

The distribution function (CDF) of U_{var} is expanded mathematically as:

$$F_{U_{var}}(y) = \Pr\left(\max\left(\Gamma_{D_1}, \Gamma_{AF,D_1}^{S_1}\right) < y\right)$$
$$= 1 - e^{-\frac{\eta_{D_1}}{\alpha_1\bar{\gamma}}y} \sum_{t=0}^{\kappa_{D_1}-1} \frac{\eta_{D_1}^t y^t}{t!\,(\alpha_1\bar{\gamma})^t} \Bigg[1 - 2 \sum_{p=0}^{\kappa_{AF}K-1} \sum_{w=0}^{p} \sum_{l=0}^{\kappa_{AF,D_1}K-1} \binom{p}{w}$$
$$\times \binom{\kappa_{AF,D_1}K-1}{l} \frac{\eta_{AF,D_1}^{\kappa_{AF,D_1}K} \eta_{AF}^p e^{-\frac{y}{\alpha_1\bar{\gamma}}(\eta_{AF,D_1}+\eta_{AF})}}{p!\,\Gamma\left(\kappa_{AF,D_1K}\right)\left(\frac{y}{\alpha_1\bar{\gamma}} + \bar{\gamma}^{-1}\right)^w}$$
$$\times \left(1 - e^{-\frac{\eta_{D_1}}{\alpha_1\bar{\gamma}}y} \sum_{t=0}^{\kappa_{D_1}-1} \frac{\eta_{D_1}^t y^t}{t!\,(\alpha_1\bar{\gamma})^t}\right) \left(\frac{\eta_{AF}}{\eta_{AF,D_1}\alpha_1\bar{\gamma}}\left(\frac{y}{\alpha_1\bar{\gamma}} + \bar{\gamma}^{-1}\right)y\right)^{\frac{l-w+1}{2}}$$
$$\times \left(\frac{y}{\alpha_1\bar{\gamma}}\right)^{\kappa_{AF,D_1}K+p-l-1} K_{l-w+1}\left(2\sqrt{\frac{\eta_{AF}\eta_{AF,D_1}}{\alpha_1\bar{\gamma}}\left(\frac{y}{\alpha_1\bar{\gamma}} + \bar{\gamma}^{-1}\right)y}\right)\Bigg] \tag{28}$$

Applying (28) into (27), we partition C_{D_1} into two sub-integrals:

$$C_{D_1} = \frac{1}{2\ln 2}\left(I_{sub1} + I_{sub2}\right) \tag{29}$$

where the first piece acts as:

$$I_{sub1} = \sum_{t=0}^{\kappa_{D_1}-1} \frac{\eta_{D_1}^t}{t!\,(\alpha_1\bar{\gamma})^t} \int_0^\infty \frac{y^t e^{-\frac{\eta_{D_1}}{\alpha_1\bar{\gamma}}y}}{1+y}\,dy \tag{30}$$

Translating this through Meijer-G function properties yields:

$$I_{sub1} = \sum_{t=0}^{\kappa_{D_1}-1} \frac{\eta_{D_1}^t}{t!\,(\alpha_1\bar{\gamma})^t} G_{1,2}^{2,1}\left(\frac{\eta_{D_1}}{\alpha_1\bar{\gamma}}y \middle| \begin{matrix} 1-t-1, - \\ 1-t-1, 0 \end{matrix}\right) \tag{31}$$

Correspondingly, the second integral segment I_{sub2} emerges as:

$$I_{sub2} = 2 \sum_{p=0}^{\kappa_{AF}K-1} \sum_{w=0}^{p} \sum_{l=0}^{\kappa_{AF,D_1}K-1} \binom{p}{w} \binom{\kappa_{AF,D_1}K-1}{l} \frac{\eta_{AF,D_1}^{\kappa_{AF,D_1}K} \eta_{AF}^p}{p!\,\Gamma\left(\kappa_{AF,D_1}K\right)}$$
$$\times \int_0^\infty \frac{1}{1+y}\left(1 - e^{-\frac{\eta_{D_1}}{\alpha_1}y} \sum_{t=0}^{\kappa_{D_1}-1} \frac{\eta_{D_1}^t y^t}{t!\,(\alpha_1\bar{\gamma})^t}\right)\left(\frac{y}{\alpha_1\bar{\gamma}} + \bar{\gamma}^{-1}\right)^w$$
$$\times \left(\frac{y}{\alpha_1\bar{\gamma}}\right)^{\kappa_{AF,D_1}K+p-l-1} \left(\frac{\eta_{AF}}{\eta_{AF,D_1}}\left(\frac{y}{\alpha_1\bar{\gamma}} + \bar{\gamma}^{-1}\right)y\right)^{\frac{l-w+1}{2}}$$
$$\times e^{-\frac{y}{\alpha_1\bar{\gamma}}(\eta_{AF,D_1}+\eta_{AF})} K_{l-w+1}\left(2\sqrt{\eta_{AF}\eta_{AF,D_1}\left(\frac{y}{\alpha_1\bar{\gamma}} + \bar{\gamma}^{-1}\right)y}\right)dy \tag{32}$$

Adopting the Gaussian-Chebyshev node methodology to bypass intractability, I_{sub2} closely approximates to:

$$I_{sub2} \approx \frac{\pi^2}{2J} \sum_{p=0}^{\kappa_{AF}K-1} \sum_{w=0}^{p} \sum_{l=0}^{\kappa_{AF,D_1}K-1} \sum_{j=1}^{J} \binom{p}{w} \binom{\kappa_{AF,D_1}K-1}{l} \frac{\eta_{AF,D_1}^{\kappa_{AF,D_1}K} \eta_{AF}^p}{p!\,\Gamma\left(\kappa_{AF,D_1}K\right)}$$
$$\times \frac{\sqrt{1-\chi_j^2}}{1+\Upsilon(\chi_j)}\left(1 - e^{-\eta_{D_1}\Xi(\chi_j)} \sum_{t=0}^{\kappa_{D_1}-1} \frac{\eta_{D_1}^t\,\Xi(\chi_j)^t}{t!}\right)$$

$$\times \sec^2\left(\frac{\pi}{4}\left(\Upsilon(\chi_j)+1\right)\right)\left(\Xi(\chi_j)+\bar{\gamma}^{-1}\right)^{w} e^{-\Xi(\chi_j)(\eta_{AF,D_1}+\eta_{AF})}$$

$$\times \Xi(\chi_j)^{\kappa_{AF,D_1}K+p-l-1}\left(\frac{\eta_{AF}\Pi(w)}{\eta_{AF,D_1}}\right)^{\frac{l-w+1}{2}} K_{l-w+1}\left(2\sqrt{\eta_{AF}\eta_{AF,D_1}\Pi(w)}\right) \quad (33)$$

in which $\chi_j = \cos\left(\frac{2j-1}{2J}\pi\right), \Upsilon(x) = \tan\left(\frac{\pi(x+1)}{4}\right), \Xi(x) = \frac{\Upsilon(x)}{\alpha_1\bar{\gamma}}$ and the term $\Pi(x) = \Xi(x)(\Xi(x) + \bar{\gamma}^{-1})$. Combining these solves C_{D_1} fully.

4. SIMULATION RESULTS

Within this section, we validate the derived analytical models through extensive numerical simulations. For simplicity across all evaluation scenarios, we assume a uniform fading severity environment by configuring the shape parameter as $\kappa = \kappa_{D_1} = \kappa_{D_2} = \kappa_{AF} = \kappa_{AF,D_1} = \kappa_{AF,D_2}$.

For clarity, this assumption is adopted to highlight the impact of key system parameters, such as the transmit SNR and the number of relay antennas. Nevertheless, in practical wireless environments, different communication links may experience heterogeneous fading conditions due to varying propagation characteristics (e.g., line-of-sight and non-line-of-sight components). It is important to emphasize that the proposed analytical framework does not rely on the assumption of identical fading parameters and the derived expressions remain valid when each link is characterized by a distinct Nakagami fading severity parameter κ. The use of a common κ value is therefore mainly for clarity and fair comparison purposes, while extending the analysis to heterogeneous fading scenarios is straightforward and left for future work.

The fundamental configuration metrics utilized for our network evaluation are summarized in Table 1. Furthermore, to guarantee a highly accurate evaluation of the integral approximations, the complexity terms for the Gauss-Chebyshev quadrature are fixed at $D = J = 100$.

Table 1. Summary of baseline simulation parameters.

Parameter Description	Notation	Assigned Value(s)
NOMA power allocation factors	$\{\alpha_1, \alpha_2\}$	{0.1, 0.9}
Nakagami fading-severity index	κ	2
Target SINR threshold	τ_{th}	2 (dB)
Number of antennas at the AF relay	K	{1,2,3}
Average channel-scale parameters	$\{\lambda_{D_1}, \lambda_{D_2}\}$	{1,1}
	λ_{AF}	1
	λ_{AF,D_1}	0.5
	λ_{AF,D_2}	0.9

We have verified that increasing the quadrature orders beyond these values (e.g., $J = 80,100,120$) results in negligible changes in the numerical results, thereby confirming the convergence behavior and accuracy of the adopted approximation. Specifically, the numerical computation of the ergodic capacity expressions requires $\mathcal{O}(D)$ and $\mathcal{O}(J)$ operations for the corresponding quadrature sums, while the remaining finite summations depend on the fading parameters and the number of relay antennas. Therefore, the proposed analytical evaluation remains computationally efficient and avoids the excessive runtime required by large-scale Monte-Carlo simulations. Specifically, the overall complexity scales linearly with the quadrature orders, i.e., $\mathcal{O}(D)$ or $\mathcal{O}(D + J)$ depending on the considered expressions.

Since the adopted quadrature orders are moderate (e.g., $J = 100$), the resulting computational burden remains low and tractable. Compared with conventional Monte-Carlo simulations, which typically require a large number of channel realizations to achieve statistical accuracy, the proposed analytical

approach significantly reduces computational cost while maintaining high accuracy. Therefore, the adopted approximation method provides an efficient and practical means for performance evaluation.

Fig. 2 depicts the system's outage probability as a function of the transmit SNR, $\bar{\gamma}$, across varying antenna-array sizes at the relay, K. Thanks to the core power-domain NOMA allocation rules, the far destination, D_2, inherently experiences superior outage reliability compared to the near destination, D_1. At lower $\bar{\gamma}$ regimes (between 0 and 10 dB), D_2 's outage rate stays practically at 10^0, reflecting a state dominated by noise and inter-user interference. However, as $\bar{\gamma}$ scales up, a sharp decline in outage probability is noticeable for both nodes, showcasing a much steeper decay at elevated SNR levels. Additionally, scaling the relay antenna count from $K = 1$ to $K = 3$ drastically mitigates outage events, verifying that augmented spatial diversity inherently fortifies the overall transmission robustness.

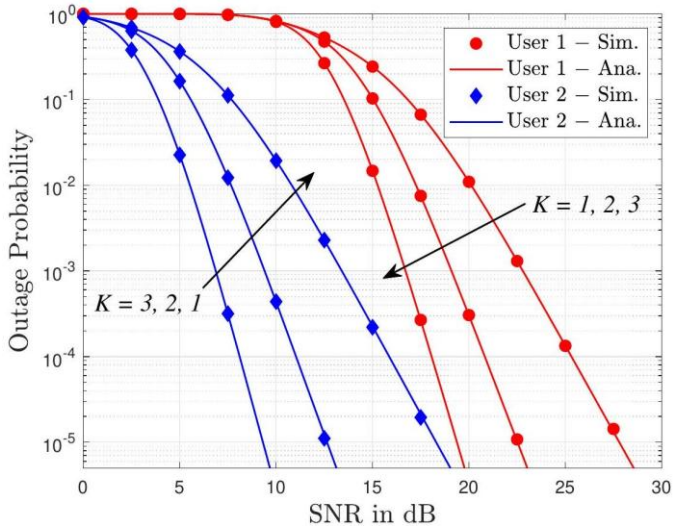

Figure 2. Outage probability *versus* transmitting SNR of two users.

Fig. 3 investigates the influence of the Nakagami fading severity index, κ, on the outage probability against $\bar{\gamma}$ when the relay is equipped with $K = 2$ antennas. Similar to previous observations, D_2 consistently preserves a lower outage profile than D_1 regardless of the transmission power. Naturally, higher $\bar{\gamma}$ translates to rapid drops in communication failures. Notably, boosting the shape parameter κ causes the performance curves to drop more precipitously, which implies a direct enhancement in the system's diversity order. Such trends perfectly align with the closed-form mathematics established earlier, confirming that higher κ values-indicative of less destructive fading conditions-yield substantially better reliability.

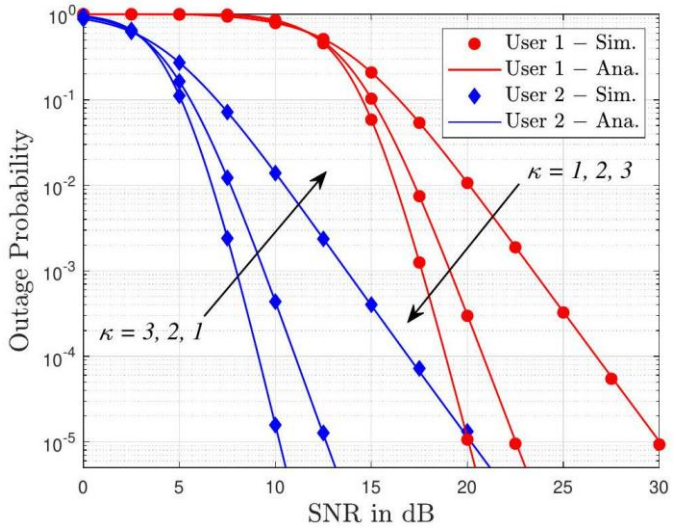

Figure 3. The outage probability *versus* SNR and different values of κ, with $K = 2$.

The impact of the power sharing factor, α_2, on the outage behavior is captured in Fig. 4, under a fixed $\bar{\gamma} = 15$ dB, $\kappa = 2$ and assorted K configurations. It is evident that dedicating a larger power fraction to

D_2 (increasing α_2) smoothly diminishes its probability of outage. Conversely, this exact increment starves D_1 of transmit power, consequently inflating its outage probability. This divergence perfectly encapsulates the fundamental power-domain compromises essential to NOMA frameworks. As expected, irrespective of the power split, expanding the relay's antenna array (K) continually upgrades both users' resilience by virtue of amplified spatial diversity gains.

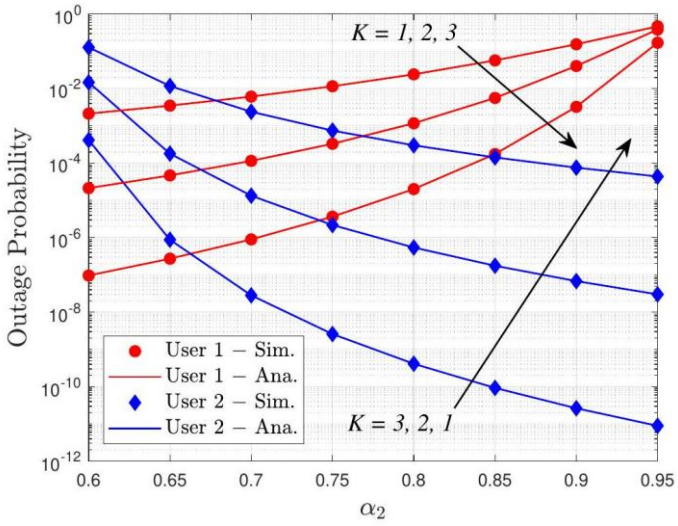

Figure 4. The outage probability *versus* α_2 with $\bar{\gamma} = 15(\text{ dB}), \kappa = 2$ and different values of K.

Fig. 5 contrasts the outage outcomes between network topologies that incorporate a direct $S \to D_i$ link *versus* those that strictly rely on the relay, evaluated at $\tau_{th} = 3$ dB and $K = 2$. Driven by the NOMA power-allocation hierarchy, D_2 constantly outshines D_1 in terms of reliability. Removing the direct transmission paths noticeably deteriorates the performance for both destinations, underscoring the critical advantage of leveraging the extra spatial diversity path. Moreover, transitioning the fading profile from $\kappa = 1$ to $\kappa = 2$ yields remarkable reliability upgrades in both topological setups, as milder fading intrinsically fortifies signal integrity.

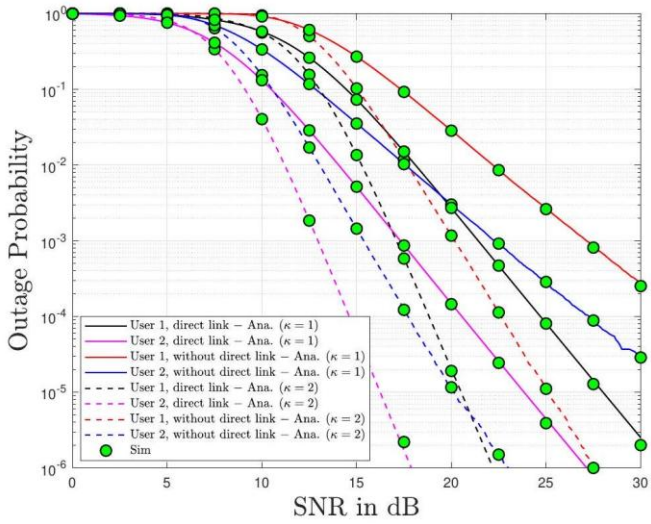

Figure 5. The outage probability with/without direct link *versus* $\tau_{\text{th}} = 3(\text{ dB}), \alpha_1 = 0.2$ and $K = 2$.

To provide meaningful and controlled baseline comparisons, the simulations evaluate the proposed NOMA scheme against OMA transmission, relay-assisted scenarios with and without direct links and different relay antenna configurations. These baselines are carefully selected to isolate the individual performance gains arising from power-domain multiplexing, cooperative relaying and spatial diversity. It is worth noting that the considered multi-antenna AF relaying framework serves as a fundamental benchmark for cooperative communication systems. While more advanced technologies, such as decode-and-forward relaying, reconfigurable intelligent surfaces and rate-splitting multiple access may

offer additional performance improvements, their integration typically requires substantially different system models and optimization strategies. Therefore, such comparisons are left for future work.

A direct reliability comparison between the proposed NOMA strategy and a conventional OMA baseline is portrayed in Fig. 6. The graphical data confirms that, for both $K = 1$ and $K = 2$ setups, the NOMA paradigm affords D_2 a noticeably lower outage probability than OMA. On the flip side, the near user (D_1) generally experiences better outage conditions under the OMA scheme than NOMA. Universally, elevating $\bar{\gamma}$ guarantees a swift plunge in the outage curves across all evaluated scenarios.

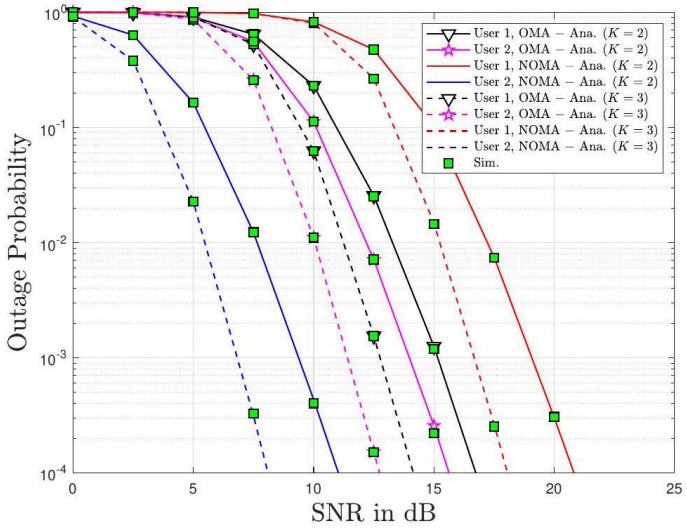

Figure 6. Comparison of outage probability between OMA and NOMA *versus* SNR, with $\kappa = 2$.

Fig. 7 plots the ergodic capacity trends against $\bar{\gamma}$ for varied relay antenna array dimensions ($K = 2,4,6$) while $\kappa = 2$. Analyzing the curves, D_2 's capacity climbs steadily within the low-to-medium $\bar{\gamma}$ bracket ($0 - 30$ dB), yet it begins to hit a ceiling at higher transmission powers. This saturation plateau occurs, because D_2 's throughput is heavily bottlenecked by inter-user interference and the fixed power allocation of NOMA. D_1, in stark contrast, enjoys an unabated capacity surge in the high- $\bar{\gamma}$ regime, thoroughly capitalizing on SIC mechanisms and amplified signal vigor. Equipping the relay with more antennas systematically elevates the ergodic capacity bounds for both nodes, thanks to superior spatial diversity. Nevertheless, for D_2, the added value of larger K arrays diminishes at high $\bar{\gamma}$, given that the environment shifts into an interference-limited state.

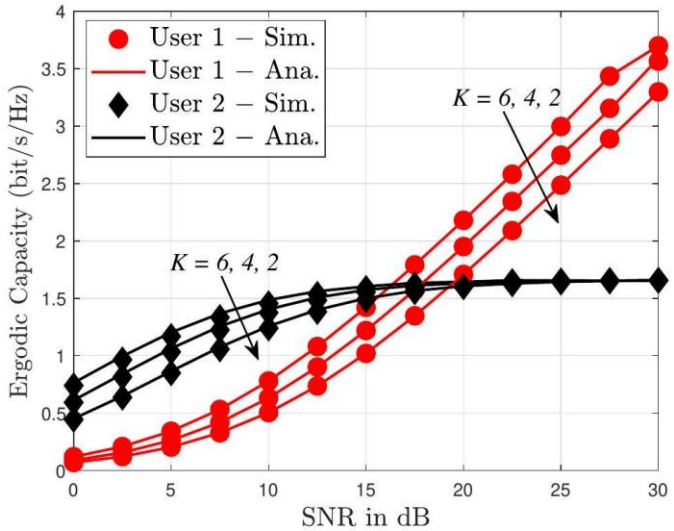

Figure 7. The ergodic capacity *versus* SNR and different values of K, with $\kappa = 2$.

Finally, Fig. 8 delineates the ergodic capacity as a function of the relay antenna count K when $\kappa = 2$. Throughout the evaluations, D_1 sustains a notably higher capacity output than D_2. Expanding K triggers substantial capacity boosts for D_1, a direct byproduct of the pronounced array and diversity gains

afforded by the multi-antenna relay. For D_2, however, the capacity only registers marginal improvements, effectively plateauing once K surpasses four antennas. This physical constraint aligns seamlessly with the derived analytical capacity equations, confirming that D_2 's upper bounds are dictated largely by NOMA power thresholds and persisting interference, thus capping the dividends paid by massive antenna expansions.

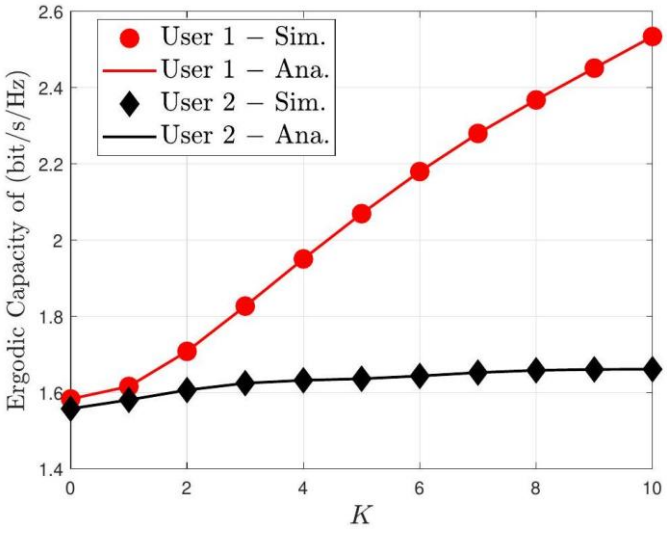

Figure 8. The ergodic capacity *versus* K, with $\kappa = 2$.

Although the analytical results are derived under the ideal SIC assumption, the impact of imperfect SIC can be interpreted as a degradation in the effective SINR due to residual interference, which results in a performance loss in terms of outage probability and ergodic capacity. However, the overall trends observed in the simulations remain unchanged.

5. CONCLUSIONS

This paper has analyzed a downlink cooperative NOMA system assisted by a multi-antenna amplify-and-forward relay over independent Nakagami- κ fading channels, where both direct and relay-assisted transmission links were considered. Closed-form expressions for the outage probability and ergodic capacity of both users were derived, providing an exact performance characterization.

The results show that employing multiple relay antennas significantly improves reliability by exploiting spatial diversity, leading to substantial outage reduction in the high-SNR region. The presence of direct BS-user links further enhances performance through selection combining. In addition, the proposed NOMA scheme outperforms OMA in terms of outage performance for the far user while achieving noticeable ergodic capacity gains at moderate-to-high SNR levels.

These findings confirm the effectiveness of multi-antenna AF relaying in enhancing reliability and spectral efficiency for cooperative NOMA systems. Future work may further consider more practical system impairments and asymmetries, including imperfect SIC, heterogeneous noise levels and link-specific path-loss conditions, to extend the proposed framework toward more realistic deployment scenarios. Future work may extend the current framework to incorporate more advanced communication paradigms, such as RIS-assisted transmission, DF relaying strategies and rate-splitting multiple access, to further enhance system performance under more complex network architectures.

APPENDICES

Appendix A - Proof of Proposition 1

Starting from the outage baseline, D_2 's probability of failure decomposes into:

$$O_2 = \underbrace{\Pr\left(\frac{\alpha_2 \bar{\gamma} W_2}{\alpha_1 \bar{\gamma} W_2 + 1} < \tau_{th}\right)}_{\Psi_1} \underbrace{\Pr\left(\Gamma_{AF,D_2}^{S_2} < \tau_{th}\right)}_{\Psi_2}. \quad (A.1)$$

Solving for Ψ_1

Analyzing the direct interference constraint:

$$\frac{\alpha_2 \bar{\gamma} W_2}{\alpha_1 \bar{\gamma} W_2 + 1} < \tau_{th}$$

we can isolate the channel gain requirement as:

$$W_2 < \vartheta,$$

assuming the boundary condition $\alpha_2 > \alpha_1\tau_{th}$ to prevent infinite thresholding, where:

$$\vartheta = \frac{\tau_{th}}{\bar{\gamma}(\alpha_2 - \alpha_1\tau_{th})}$$

This immediately confirms:

$$\Psi_1 = F_{W_2}(\vartheta) = 1 - e^{-\eta_{D_2}\vartheta}\sum_{u=0}^{\kappa_{D_2}-1}\frac{\eta_{D_2}^u\vartheta^u}{u!} \quad (A.2)$$

Solving for Ψ_2

Recalling the relayed SINR equation, the condition $\Gamma_{AF,D_2}^{S_2} < \tau_{\text{th}}$ is mathematically equivalent to bounding V:

$$VQ_2 < \vartheta(V + Q_2 + \bar{\gamma}^{-1}).$$

Restructuring provides:

$$V < \frac{\vartheta(Q_2 + \bar{\gamma}^{-1})}{Q_2 - \vartheta}, Q_2 > \vartheta.$$

Integrating over the PDF of Q_2 grants:

$$\Psi_2 = 1 - \int_{\vartheta}^{\infty} f_{Q_2}(y)\left[1 - F_V\left(\frac{\vartheta(y + \bar{\gamma}^{-1})}{y - \vartheta}\right)\right]dy \quad (A.3)$$

By expanding the probability definitions, Ψ_2 forms into:

$$\Psi_2 = 1 - \sum_{v=0}^{\kappa_{AF}K-1}\frac{\eta_{AF,D_2}^{\kappa_{AF,D_2}K}\eta_{AF}^v}{v!\,\Gamma(\kappa_{AF,D_2}K)}\int_{\vartheta}^{\infty} y^{\kappa_{AF,D_2}K-1}e^{-\eta_{AF,D_2}y}e^{-\eta_{AF}\frac{\vartheta(y+\bar{\gamma}^{-1})}{y-\vartheta}}\left(\frac{\vartheta(y + \bar{\gamma}^{-1})}{y - \vartheta}\right)^v dy \quad (A.4)$$

Applying a lateral shift $z = y - \vartheta$, the expression updates to:

$$\Psi_2 = 1 - \sum_{v=0}^{\kappa_{AF}K-1}\frac{\eta_{AF,D_2}^{\kappa_{AF,D_2}K}\eta_{AF}^v e^{-\vartheta\left(\eta_{AF,D_2}+\eta_{AF}\right)}}{v!\Gamma(\kappa_{AF,D_2}K)}\int_0^{\infty}(z+\vartheta)^{\kappa_{AF,D_2}K-1}e^{-\eta_{AF,D_2}z}e^{-\frac{\eta_{AF}\vartheta(\vartheta+\bar{\gamma}^{-1})}{z}}\left(\vartheta + \frac{\vartheta^2+\vartheta\bar{\gamma}^{-1}}{z}\right)^v dz.$$

Evaluating the integration parameters using Bessel transformation rules concludes the proof mapping identically to (17).

Appendix B - Proof of Proposition 2

Beginning with the integral definition of capacity for D_2 :

$$C_{D_2} = \mathbb{E}\left\{\frac{1}{2}\log_2\left(1 + \Gamma_{D_2}^{eff}\right)\right\} = \frac{1}{2\ln 2}\int_0^{\frac{\alpha_2}{\alpha_1}}\frac{1}{1+y}\left[1 - F_{X_{tmp}}\left(\frac{y}{\alpha_2 - \alpha_1 y}\right)\right]dy \quad (B.1)$$

Undergoing the variable conversion $z = \frac{y}{\alpha_2 - \alpha_1 y}$, (B.1) translates to:

$$C_{D_2} = \frac{1}{2\ln 2}\int_0^{\infty}\left(\frac{1}{z + (\alpha_2 + \alpha_1)^{-1}} - \frac{1}{z + \alpha_1^{-1}}\right)\left[1 - F_{X_{tmp}}(z)\right]dz \quad (B.2)$$

Linking back to the outage-probability derivations, $F_{X_{tmp}}(z)$ incorporates both direct and relayed elements, culminating in:

$$C_{D_2} = \frac{1}{2\ln 2}(\Delta_1 + \Delta_2) \quad (B.3)$$

Here, Δ_1 handles the un-relayed components:

$$\Delta_1 = \sum_{u=0}^{\kappa_{D_2}-1}\frac{\eta_{D_2}^u}{u!\,\bar{\gamma}^u}\int_0^{\infty}\left(\frac{1}{z + (\alpha_2 + \alpha_1)^{-1}} - \frac{1}{z + \alpha_1^{-1}}\right)z^u e^{-\frac{\eta_{D_2}}{\bar{\gamma}}z}dz \quad (B.4)$$

Transforming the exponential component using $e^{-bz} = G_{0,1}^{1,0}\left(bz\middle|\begin{matrix}-\\0\end{matrix}\right)$, Δ_1 is computed strictly as:

$$\Delta_1 = \sum_{u=0}^{\kappa_{D_2}-1}\frac{\eta_{D_2}^u}{u!\,\bar{\gamma}^u}\left[\frac{1}{(\alpha_2 + \alpha_1)^u}G_{1,2}^{2,1}\left(\frac{\eta_{D_2}}{\bar{\gamma}(\alpha_2 + \alpha_1)}\middle|\begin{matrix}1-u-1,-\\1-u-1,0\end{matrix}\right) - \frac{1}{\alpha_1^u}G_{1,2}^{2,1}\left(\frac{\eta_{D_2}}{\bar{\gamma}\alpha_1^u}\middle|\begin{matrix}1-u-1,-\\1-u-1,0\end{matrix}\right)\right] \quad (B.5)$$

Meanwhile, Δ_2 dictates the relayed capacity segment, eventually resolved through numeric approximation (Gaussian-Chebyshev boundaries), completing the analysis.

REFERENCES

[1] Z. Ding et al., "A Survey on Non-orthogonal Multiple Access for 5G Networks: Research Challenges and Future Trends," IEEE Journal on Selected Areas in Communications, vol. 35, no. 10, pp. 2181-2195, 2017.

[2] L. Dai et al., "A Survey of Non-orthogonal Multiple Access for 5G," IEEE Communications Surveys & Tutorials, vol. 20, no. 3, pp. 2294-2323, 2018.

[3] Z. Wei et al., "A Survey of Downlink Non-orthogonal Multiple Access for 5G Wireless Communication Networks," arXiv preprint, arXiv: 1609.01856, 2016.

[4] S. R. Islam et al., "Power-domain Non-orthogonal Multiple Access (NOMA) in 5G Systems: Potentials and Challenges," IEEE Comm. Surveys & Tutorials, vol. 19, no. 2, pp. 721-742, 2016.

[5] Q.-S. Nguyen, T. N. Nguyen and L.-T. Tu, "On the Security and Reliability Performance of SWIPT-enabled Full-duplex Relaying in the Non-orthogonal Multiple Access Networks," Journal of Information and Telecommunication, vol. 7, no. 4, pp. 462-476, 2023.

[6] M. Zeng et al., "Cooperative NOMA: State of the Art, Key Techniques and Open Challenges," IEEE Network, vol. 34, no. 5, pp. 205-211, 2020.

[7] Y. Yuan et al., "Joint Robust Beamforming and Power-splitting Ratio Design in SWIPT-based Cooperative NOMA Systems with CSI Uncertainty," IEEE Trans. on Vehicular Technology, vol. 68, no. 3, pp. 2386-2400, March 2019.

[8] A.-T. Le, T. D. Hieu, T. N. Nguyen, T.-L. Le, S. Q. Nguyen and M. Voznak, "Physical layer security analysis for RIS-aided NOMA systems with non-colluding eavesdroppers," Computer Communications, vol. 219, pp. 194-203, Apr. 2024.

[9] T. N. Nguyen, Q.-S. Nguyen, N. M. Quan, T. V. Chien, B. V. Minh and T.-L. Thuong, "Reliability and security analysis of active RIS-assisted IoT NOMA networks over Nakagami- κ fading channels," IEEE Internet of Things Journal, Early Access, DOI:10.1109/JIOT.2025.3650486, 2026.

[10] N. Q. Sang et al, "Performance of RIS-secured short-packet NOMA systems with discrete phaseshifter to protect digital content and copyright against untrusted user," IEEE Access, vol. 13, pp. 21580-21593, 2025.

[11] V.-D. Le et al., "Enabling D2D Transmission Mode of Reconfigurable Intelligent Surfaces Aided in Wireless NOMA System," Advances in Electrical and Electronic Eng., vol. 23, no. 1, 2025.

[12] T.-H. T. Pham et al., "Performance Analysis in D2D Partial NOMA-assisted Backscatter Communication," Advances in Electrical and Electronic Eng., vol. 23, no. 3, 2025.

[13] S.-Q. Nguyen et al., "Securing Short-packet Transmissions *via* Partial NOMA: Performance Analysis under Keyhole Fading," Vehicular Communications, vol. 58, p. 100999, 2026.

[14] A. Le-Thi et al., "Power Splitting-based SWIPT in UAV-aided NOMA Systems over Nakagami-m Fading: Performance Analysis and Optimization," Wireless Networks, vol. 32, pp. 315-330, 2026.

[15] M. Tran, M. Bui Vu and S. Nguyen, "On the Performance of Active RIS-enhanced NOMA Systems with Spectrum Sharing Mechanisms," Plos One, vol. 20, no. 11, p. e0336951, 2025.

[16] S.-Q. Nguyen et al., "Securing Wireless Communications with Energy Harvesting and Multi-antenna Diversity," Jordanian Journal of Computers and Information Technology (JJCIT), vol. 11, no. 2, pp. 197-210, DOI: 10.5455/jjcit.71-1732244909, Jun. 2025.

[17] V. S. Nguyen, A. Le-Thi, V. D. Thuan, C.-B. Le, T. H. Nguyen and S.-Q. Nguyen, " Analysis of Ergodic Sum Rate in RSMA with Perfect and Imperfect SIC: A Multiple-antenna Selection Approach for Optimizing UAV Positioning," Physical Communication, vol. 72, p. 102741, 2025.

[18] N. H. Nhu et al., "Covert Communication Performance Evaluation in UAV-assisted Rate-splitting Multiple Access Systems," PLos One, vol. 20, no. 8, p. e0331013, 2025.

[19] Z. Yang, Z. Ding, Y. Wu and P. Fan, "Novel Relay Selection Strategies for Cooperative NOMA," IEEE Trans. on Vehicular Technology, vol. 66, no. 11, pp. 10114-10123, Nov. 2017.

[20] P. Xu, Z. Yang, Z. Ding and Z. Zhang, , "Optimal Relay Selection Schemes for Cooperative NOMA," IEEE Trans. on Vehicular Technology, vol. 67, no. 8, pp. 7851-7855, Aug. 2018.

[21] M. Ashraf et al., "Energy Harvesting Non-orthogonal Multiple Access System with Multi-antenna Relay and Base Station," IEEE Access, vol. 5, pp. 17660-17670, 2017.

[22] L. Lv, Q. Ye, Z. Ding, Z. Li, N. Al-Dhahir and J. Chen, "On the Design of NOMA Assisted Multi-Antenna Two-way Relay Systems," Proc. of the IEEE Int. Conf. on Communications (ICC), DOI: 10.1109/ICC40277.2020.9149110, Dublin, Ireland, 2020.

[23] X. Chen et al., "Exploiting Multiple-antenna Techniques for Non-orthogonal Multiple Access," IEEE Journal on Selected Areas in Communications, vol. 35, no. 10, pp. 2207-2220, Oct. 2017.

[24] Y. Cao et al., "Secrecy Analysis for Cooperative NOMA Networks with Multi-antenna Full-duplex Relay," IEEE Trans. on Communications, vol. 67, no. 8, pp. 5574-5587, Aug. 2019.

[25] N. Zaghdoud et al., "Secrecy Performance Analysis of Multi-antenna NOMA System with AF/DF Relaying under External and Internal Eavesdropping Scenarios," Proc. of the 2020 Int. Wireless Communications and Mobile Computing (IWCMC), pp. 1726-1732, Limassol, Cyprus, 2020.

[26] Z. Tang et al., "Reconsidering Design of Multi-antenna NOMA Systems with Limited Feedback," IEEE Trans. on Wireless Communications, vol. 19, no. 3, pp. 1519-1534, March. 2020.

[27] L. Lv, Q. Ye, Z. Ding, Z. Li, N. Al-Dhahir and J. Chen, "Multi-antenna Two-way Relay Based Cooperative NOMA," IEEE Trans. on Wireless Comm., vol. 19, no. 10, p. 64866503, 2020.

[28] T. A. Le and H. Y. Kong, "Energy Harvesting Relay-antenna Selection in Cooperative MIMO/NOMA Network over Rayleigh Fading," Wireless Net., vol. 26, no. 3, pp. 2075-2087, 2020.

[29] A. Hakimi, M. Mohammadi and Z. Mobini, "Outage Probability of Wireless-powered Multi-antenna Cooperative Spectrum Sharing Networks with Full-duplex and NOMA Transmissions," Proc. of the 2018 9th Int. Symposium on Telecommunications (IST), pp. 127-132, Tehran, Iran, 2018.

[30] Z. Mobini et al., "Full-duplex Multi-antenna Relay Assisted Cooperative Non-orthogonal Multiple Access," Proc. of the 2017 IEEE Global Communications Conference, pp. 1-7, Singapore, 2017.

[31] A. Jee and S. Prakriya, "Performance of Energy and Spectrally Efficient AF Relay-aided Incremental CDRT NOMA-based IoT Network with Imperfect SIC for Smart Cities," IEEE Internet of Things Journal, vol. 10, pp. 18766-18781, 2023.

[32] C. Hu, Q. Li, Q. Zhang and J. Qin, "Security Optimization for an AF MIMO Two-way Relay-assisted Cognitive Radio Non-orthogonal Multiple Access Networks with SWIPT," IEEE Trans. on Information Forensics And Security, vol. 17, pp. 1481-1496, 2022.

[33] I. S. Gradshteyn and I. M. Ryzhik, Tables of Integrals, Series and Products, 6th Edn., ISBN-10: 0-12-373637-4, New York: Academic Press, 2000.

[34] Q. Wang, J. Ge, Q. Li and Q. Bu, "Performance Analysis of NOMA for Multiple-antenna Relaying Networks with Energy Harvesting over Nakagami-m Fading Channels," Proc. of the 2017 IEEE/CIC Int. Conf. on Communications in China, pp. 1-5, Qingdao, China, Oct. 2017.

[35] C. C. Hung, C. T. Chiang, S. N. Lin and R. C. Wu, "Outage Capacity Analysis of TAS/MRC Systems over Arbitrary Nakagami-m Fading Channels," IEICE Trans. on Communications, vol. 93, no. 1, pp. 215-218, 2010.

ملخص البحث:

تبحث هذه الورقة في نظام الوصول المتعدّد غير المتعامِد التّعاوني (NOMA) للوصلة الهابطة، متعدّد الهوائيات، المدعوم بمرحل تضخيم وإعادة توجيه، على عكس تكوينات التّرحيل التّقليدية أحادية الهوائي.

يستغلّ الإطار المدروس تنوُّع التّرحيل وروابط الإرسال المباشر بين المحطّة الأرضية والمستخدمين. وفي ظلّ قنوات التلاشي المستقلّة، يتم اشتقاق صيغٍ مغلقة لاحتمالية انقطاع الخدمة والسّعة الإرجودية للمستخدمين في سيناريوهات وجود روابط مباشرة بين المحطّة الأساسية والمستخدمين وعدم وجودها.

ويوضّح النّموذج التّحليلي تأثير عدد هوائيات التّرحيل وشدّة التّلاشي ومعاملات تخصيص الطّاقة على أداء النّظام. ولتحليل السّعة الإرجودية، تمّ تطوير تمثيلٍ تكاملي دقيق مقترن بنهج تربيعي لتقييم الأداء بكفاءة. وقد تمّ التّحقُّق من النّتائج التّحليلية من خلال محاكاة مونت كارلو ومقارنتها بمعايير الوصول المتعدّد المتعامِد.

وأظهرت النّتائج العددية أنّ زيادة عدد هوائيات التّرحيل تحسّن الموثوقية بشكلٍ ملحوظ بفضل تعزيز التّنوُّع المكاني. علاوةً على ذلك، يحقّق نظام الوصول المتعدّد غير المتعامِد أداءً فائقاً في تقليل انقطاع الخدمة للمستخدِم البعيد مقارنةً بنظام الوصول المتعدّد المتعامِد، بينما تُظهر السّعة الإرجودية للمستخدِم القريب تحسُّناً ملحوظاً في نطاق نسبة الإشارة إلى الضّجيج المتوسّطة إلى العالية.

وتؤكّد هذه النّتائج فعالية تقنية التّرحيل التّعاوني متعدّد الهوائيات في تحسين كلٍّ من الموثوقية وكفاءة استخدام الطّيْف.